

Full Length Article

Molybdenum disulfide monolayer electronic structure information as explored using density functional theory and quantum theory of atoms in molecules

Nicholas Dimakis ^{a,*}, Om Vadodaria ^b, Korinna Ruiz ^c, Sanju Gupta ^d^a Department of Physics and Astronomy, University of Texas Rio Grande Valley, Edinburg, TX 78539, USA^b The Science Academy, Mercedes, TX 78570, USA^c South Texas High School for Health Professions, Mercedes, TX 78570, USA^d Department of Physics and NanoScience Technology Center University of Central Florida, Orlando, FL 32816, USA

ARTICLE INFO

Keywords:
 MoS₂
 Defects
 DFT
 QTAIM
 Bandgap

ABSTRACT

We use density functional theory (DFT) and quantum theory of atoms in molecules (QTAIM) to study the electronic structure of pristine and defect molybdenum disulfide (MoS₂) monolayers, at dry and hydrated conditions. We study various defect MoS₂ configurations, which are described by the presence of one or more sulfur (S) vacancies, including voids. Structural defects introduce deep and shallow defect states in the electronic band structure in the vicinity of the Fermi energy, which affect the bandgap and introduce mid-gap states. Hydration also affects the bandgap and the mid-gaps of defect MoS₂. We use QTAIM parameters at bond critical points to identify the MoS₂ bond types and their strength. QTAIM shows the presence of Mo—S and S—S bonding, the former being weakly covalent, and the latter refers to a closed shell interaction. Water and its dissociated products are strongly adsorbed on Mo atoms due to the presence of low electron density areas in the vicinity of these atoms. We finally provide a correlation between changes in the electron density at the Mo-S bond critical points around the structural defect and the mid-gap around the Fermi energy. These findings become relevant for designing electrocatalysts based on MoS₂ and two-dimensional layered systems.

1. Introduction

Among the family of van der Waal solids, two-dimensional layered materials, such as transition metal dichalcogenides (TMDs) [1], which include the naturally occurring molybdenum disulfide (MoS₂) and tungsten disulfide (WS₂), are attracting a great deal of attention for fundamental science and applications. Analogous to graphene, the MoS₂ has several interesting and diverse physical and chemical properties, including excellent mechanical strength, optical, and magnetic properties [2–4]. Additionally, the MoS₂ is gaining popularity as a low-cost catalyst for the production of hydrogen fuel through the hydrogen evolution reaction (HER) [5–7]. Thus, the MoS₂ could either supplement or substitute the existing HER catalysts of noble metals, such as elemental Pt, binary, and ternary alloys, which are expensive and prone to poisoning after continuous use [8]. It is also used as a catalyst in oil refineries for crude oil sulfur removal [9] and as a solid lubricant [10–13]. The extraction of a MoS₂ monolayer from bulk MoS₂ via

micromechanical exfoliation (analogous to graphene monolayer production from graphite) has been reported by Novoselov et al [14]. In the MoS₂ monolayer, the Mo layer is sandwiched between two S layers with the Mo atoms coordinated with six S atoms, giving rise to a 6.5 Å van der Waals gap. Both Mo and S atoms form hexagonal planes. Two or more MoS₂ monolayers stack up together via weaker van der Waals forces similar to multilayer graphene and highly oriented pyrolytic graphite.

The MoS₂ monolayer is found in two structural polytypes namely, trigonal prismatic (2H) and octahedral (1T) configuration [14,15]. The former configuration, which is the most abundant, is a semiconductor, whereas the latter 1T-MoS₂ is metallic [16]. In contrast to graphene, which is a zero-bandgap semiconductor, the pristine 2H-MoS₂ monolayer has a direct bandgap of 1.8 eV [17]. This value is decreased as more layers are added, reaching the value of 1.29 eV for bulk MoS₂ [18]. The latter bandgap is of indirect nature. Hydrogen (H₂) is considered a clean “green” and sustainable energy resource. The MoS₂ HER favorable properties are due to the presence of catalytically active S sites on Mo

* Corresponding author.

E-mail address: Nicholas.dimakis@utrgv.edu (N. Dimakis).

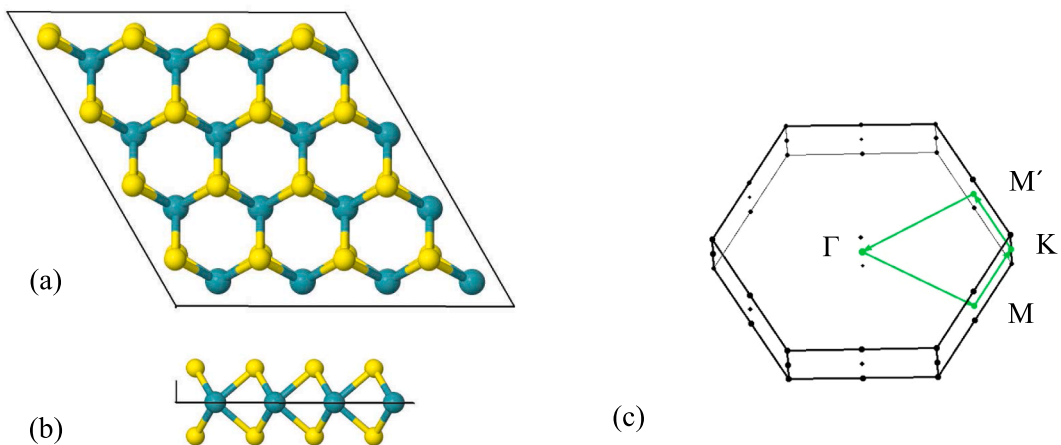


Fig. 1. The 4×4 2H-MoS₂ unit cell on a ball and stick model. (a) top and (b) side view. Atoms are colors as follows: S, yellow; Mo, green. (c) First BZ of the hexagonal lattice with the symmetry points. Visualization is via Jmol. (For interpretation of the references to colour in this figure legend, the reader is referred to the web version of this article.)

edges [19]. Hinnemann et al. using density functional theory (DFT) calculations showed that these edge S atoms are unsaturated and the free energy of hydrogen adsorption (ΔG_H) is ≈ 0.08 eV. This energy value is close to thermo-neutral, making MoS₂ potentially a promising inorganic catalyst for clean hydrogen fuel production [6]. This prediction was experimentally confirmed on MoS₂ nanoparticles, where a linear correlation between the exchange current density and MoS₂ edge length was elucidated [6]. Alternatively, the HER activity is increased via activation of the MoS₂ inert basal plane through the presence of S vacancy defects [20]. Here, we find that these defects introduce mid-gaps (i.e., energy gaps between defect states) in the Fermi energy area and thus, can tune the 2H-MoS₂ monolayer optical bandgap, thereby can also be useful for photo-assisted catalysis. Fan et al., [21] stated that the very small bandgaps of the 1T'-MoS₂ (0.1–0.2 eV) contributed to its high conductivity and thus, its function as a potential HER catalyst.

Several DFT calculations on dry pristine and defect MoS₂ monolayers [5,22–25] and multilayers [26–28] have been performed in the past. Kadantsev and Hawrylak confirmed that the dry pristine 2H-MoS₂ is a

direct bandgap $K \rightarrow K$ semiconductor [22]. Qiu et al. [23] found that single S vacancy defects on dry MoS₂ introduce defect states in the bandgap area. These defect states were observed as flat bands, with two degenerate bands at the Γ point above the Fermi energy and one band below the Fermi level and close to the top of the valence bands. The defect bands closer to the conduction band bottom are deep donor states, whereas the defect band close to the top of the valence band is a shallow donor state. He et al. [29] found that bandgap engineering of multilayer MoS₂ is feasible by introducing S vacancies of various concentrations. Li et al. [30] found that the defect gap states in the Fermi energy area are responsible for hydrogen adsorption on the exposed Mo atoms in the cases of S vacancies. However, the adsorption of small molecules, including water, on pristine MoS₂ is weak [24].

The quantum theory of atoms in molecules (QTAIM) has been developed by Bader and co-workers and it is based on the topology of electron density $\rho(\vec{r})$ and its Laplacian $\nabla^2 \rho(\vec{r})$ to describe atoms and bonding in chemical systems [31,32]. QTAIM can be used to identify the

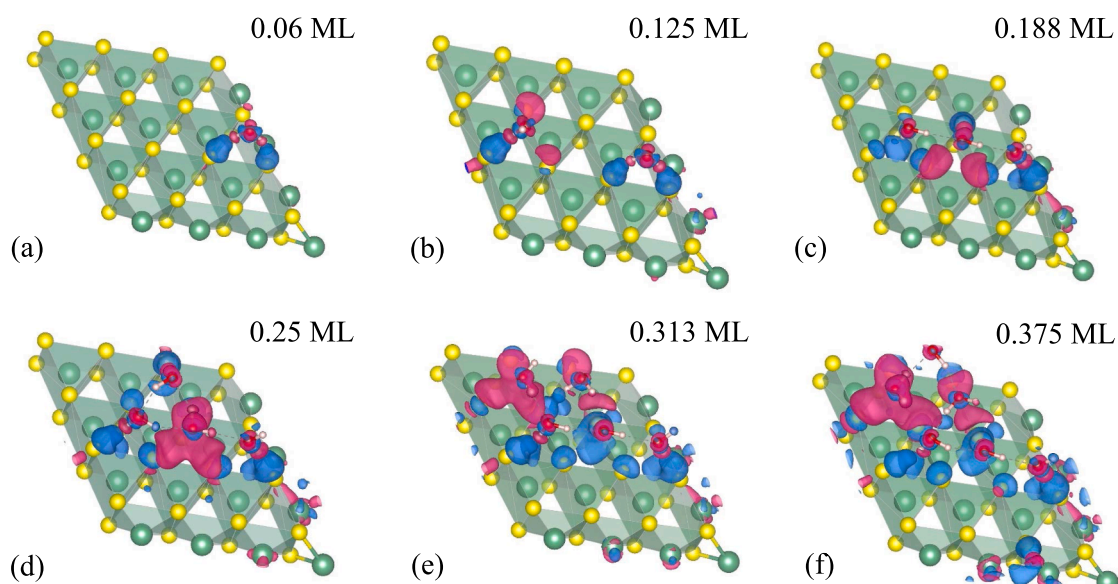


Fig. 2. Charge redistributions $\Delta\rho(\vec{r})$ for hydrated pristine MoS₂ at various water coverages (a)–(f), plotted via VESTA. Atoms are colors as follows: S, yellow; Mo, green; O, red; H, white. Blue and magenta isospheres correspond to areas of charge accumulation and depletion, respectively. Isodensity surfaces of 0.001 e/bohr³ are displayed. (For interpretation of the references to colour in this figure legend, the reader is referred to the web version of this article.)

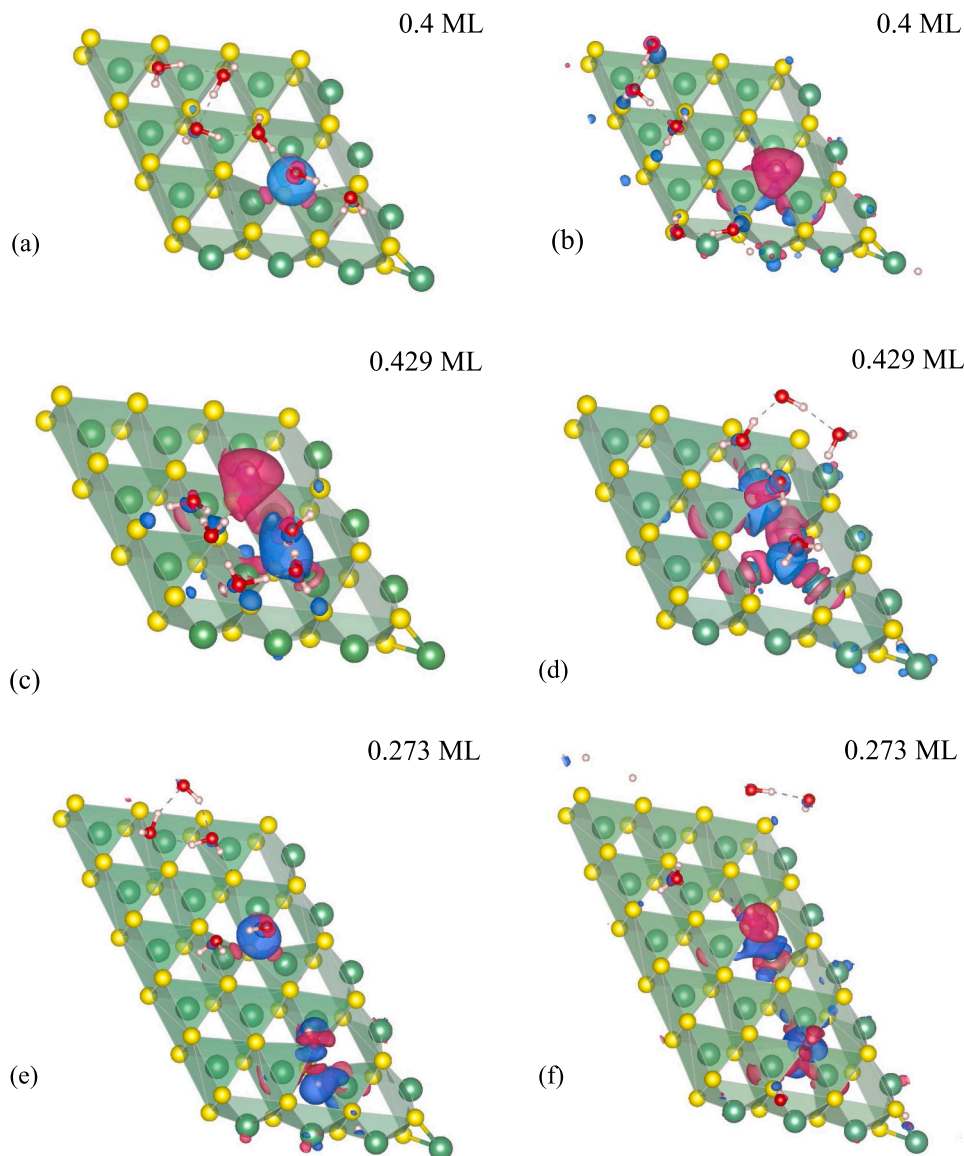


Fig. 3. Charge redistributions $\Delta\rho(\vec{r})$ for hydrated pristine MoS_2 at various water coverages and vacancy formations, plotted via VESTA. (a) Single S vacancy, (b) single S void, (c) adjacent double S vacancies, (d) adjacent double S voids, (e) non-adjacent double S vacancies, and (f) non-adjacent double S voids. Atoms are colors as follows: S, yellow; Mo, green; O, red; H, white. Blue and magenta isospheres correspond to areas of charge accumulation and depletion, respectively. Isodensity surfaces of $0.005 \text{ e}/\text{bohr}^3$ are displayed. (For interpretation of the references to colour in this figure legend, the reader is referred to the web version of this article.)

bonding type between two atoms (i.e., covalent, closed shell, etc.) [33]. QTAIM does not involve atomic or molecular orbital concepts and is characterized by changes in the $\rho(\vec{r})$ and its derivatives at critical points (cp). Specifically, there are four types of stable critical points with three non-zero eigenvalues (i.e., rank 3): (3, -3), nuclear critical points, where $\rho(\vec{r})$ is maximum; (3, -1), bond critical points, where $\rho(\vec{r})$ is maximum at a plane defined by two eigenvectors and minimum along the axis defined by the third eigenvector; (3, +1), ring critical points, where $\rho(\vec{r})$ is minimum at a plane defined by two eigenvectors and maximum along the axis defined by the third eigenvector, in an opposite fashion as the (3, -1) critical point; and (3, +3), cage critical points, where $\rho(\vec{r})$ is minimum. The presence of a bond critical point (bcp) is a necessary condition for bonding between two atoms [34]. The electron density and its derivatives are quantum observables. QTAIM analyses are basis set and method independent, as long as a minimally adequate basis set is used [35]. QTAIM on dry MoS_2 has been reported [36–38]. Aray and Rodríguez [36] examined the nature of the MoS_2 catalyst edge using QTAIM. The authors found a relationship between the energy needed to create a S vacancy with the QTAIM polyhedral defining the surface graph.

Our current work explores the changes in the electron density of

states (DOS) and band structure due to the presence of single, double, and four S vacancies in the MoS_2 lattice, as well as, due to hydration. This is an expansion of our recent experimental and computational work on MoS_2 , where we reported DFT optimized geometries and partial charges for pristine and defect 2H- MoS_2 with and without a graphene underlayer [5]. We use QTAIM analysis to examine the Mo-S bonds types and strengths and obtain QTAIM molecular graphs, which describe the MoS_2 bonding arrangement. We finally correlate the changes in the $\rho(\vec{r})$ at Mo-S bond critical points in the local area of the S defect with changes in the mid-gaps. There are past reports on correlations between QTAIM calculated properties and bandgaps [39–41]. Syzgantseva and Syzgantseva described a correlation between electron density values at bond critical points with bandgaps for perovskites [39]. Seriani reported a linear relationship between kinetic energy density at bond critical points and bandgap values for alkali and alkaline-earth oxides [40]. Kang [41] reported a correlation between the bandgap divided by the kinetic energy density and electronegativities for alkali, alkaline-earth, and rutile binary oxides. However, we are not aware of past reports ascribing changes in the mid-gaps due to defects in layered systems with QTAIM properties.

2. Computational methods

2.1. Periodic slab modelling

Fig. 1 shows the DFT optimized unit cell of the pristine 2H-MoS₂ and its first Brillouin zone (BZ). As stated previously [5], the 2H-MoS₂ is mainly modeled as two-dimensional 4 × 4 hexagonal lattice with 16 atoms per layer. A larger 4 × 6 supercell is used to model the 2H-MoS₂ configuration with non-adjacent S vacancies (24 atoms per layer in its pristine configuration). We consider the following 2H-MoS₂ defect configurations: 1) single S vacancy and adjacent and non-adjacent double S vacancies, all located at the top S layer, 2) double S vacancies, with one of the vacancies on the top layer and the other on the opposite side of the monolayer, thus forming a void and 3) four-S vacancies forming two voids (adjacent and non-adjacent). In all cases, we also examine the effects of hydration by allowing waters molecules to be adsorbed on the top S layer. Charge redistributions, due to hydration, are analyzed using the charge density differences

$$\Delta\rho(\vec{r}) = \rho_{MoS_2+Waters}(\vec{r}) - \rho_{MoS_2}(\vec{r}) - \rho_{Waters}(\vec{r}) \quad (1)$$

where $\rho_{MoS_2+Waters}(\vec{r})$, $\rho_{MoS_2}(\vec{r})$, and $\rho_{Waters}(\vec{r})$ are the charge density distributions in real space of the hydrated MoS₂, the isolated MoS₂, and the isolated water molecules, respectively. The

$\Delta\rho(\vec{r})$ of Eq. (1) are visualized using VESTA [42]. Figs. 2 and 3 show the charge redistributions due to hydration for pristine and defect MoS₂, respectively.

2.2. DFT parameters

The parameters for the periodic DFT calculations have been described previously [5] and are summarized here. The periodic DFT code CRYSTAL17 [43] was used to calculate structural and electronic information of pristine and defect MoS₂ (dry and hydrated). Both the PBE0 [44,45] and the HSE06 [46] hybrid functionals were used, the latter for providing improved bandgaps. Since DFT calculations are functional dependent, the use of two functionals allow us to identify if

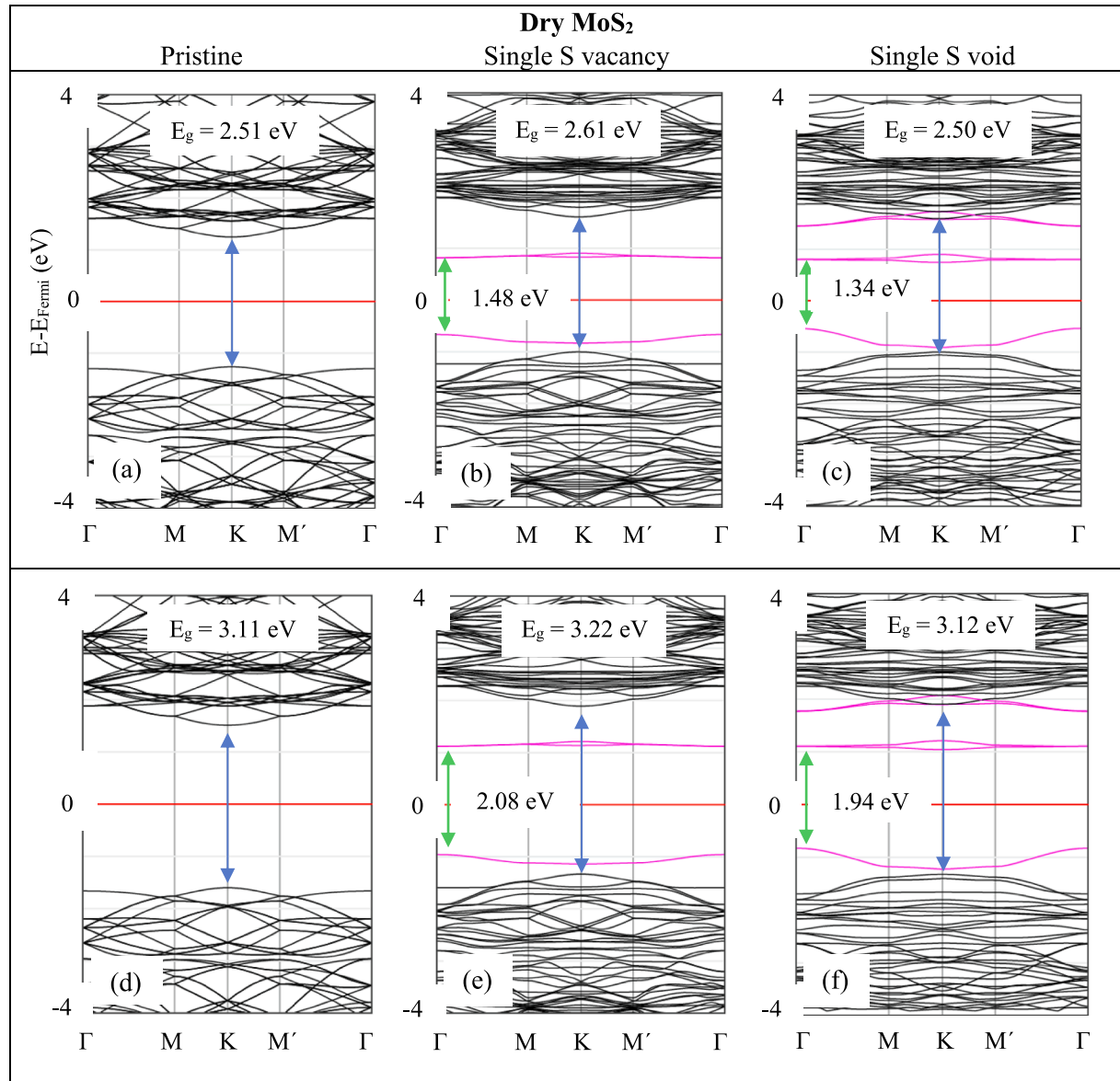


Fig. 4. Band structure for the optimized geometries under the HSE06 (a)–(c) and the PBE0 (d)–(f) functionals. Purple bands are defect bands. Blue and green arrows show bandgaps (E_g) and sub-band gaps, respectively. Red solid horizontal lines are the Fermi energies (E_{Fermi}). (For interpretation of the references to colour in this figure legend, the reader is referred to the web version of this article.)

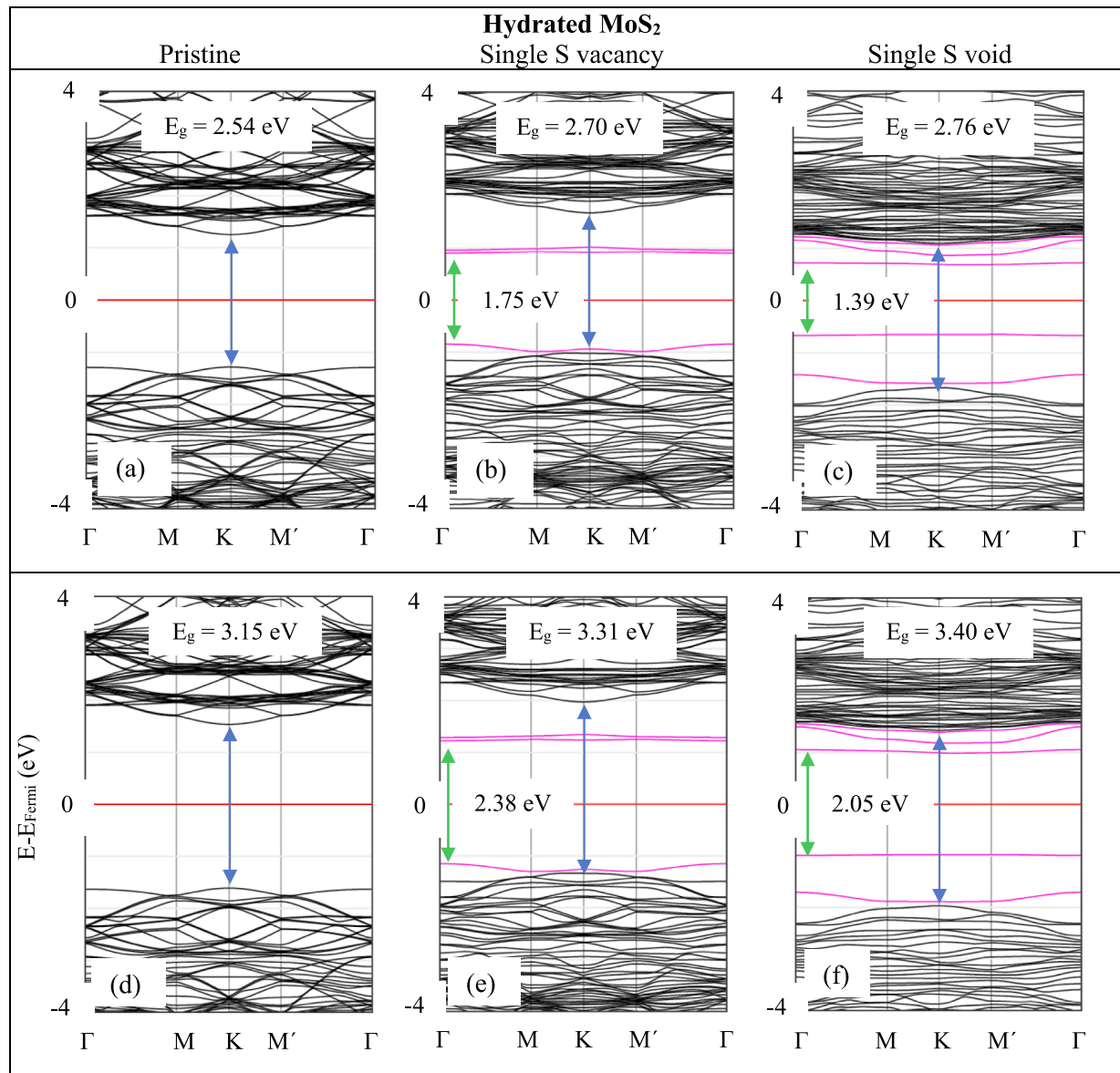


Fig. 5. Band structure for the optimized geometries under the HSE06 (a)–(c) and the PBE0 (d)–(f) functionals. Purple bands are defect bands. Blue and green arrows show bandgaps (E_g) and mid-band gaps, respectively. Red solid horizontal lines are the Fermi energies (E_{Fermi}). (For interpretation of the references to colour in this figure legend, the reader is referred to the web version of this article.)

changes in the calculated properties are systematic. Long-range electron correlations have been accounted by using the Grimme D3 correction [47]. The S, O, and H atoms were using the all-electron basis sets (pob-TZVP for S and H [48] and 8-411G(2d1f) for O [49]). The Mo atoms use effective core potentials (ECP) and their valence is described by the (3s2p2d1f) basis set [50]. The 12×12 Monkhorst-Pack [51] grid was used for geometry optimizations and BZ integrations, whereas the DOS and the electronic band structures were obtained using the denser 24×24 grid.

For band structure calculations, the BZ path Γ -M-K- \bar{M} - Γ is used (i.e., Γ , (0, 0, 0); M, (1/2, 0, 0); K, (1/3, 1/3, 0); \bar{M} = (0, 1/2, 0), see Fig. 1c).

2.3. QTAIM parameters

QTAIM provides information about the bonding strength and type between two atoms. The sign of the $\nabla^2\rho(\vec{r})$ at the bond critical point (3, -1) can be used to identify the type of the bonding: $\nabla^2\rho(\vec{r}) < 0$ for non-

polar covalent bonding and $\nabla^2\rho(\vec{r}) > 0$ for closed shell interactions and polar covalent bonding. QTAIM measures bond strengths via $\rho(\vec{r})$, $\nabla^2\rho(\vec{r})$, and $(H/\rho)(\vec{r})$ at the bond critical point \vec{r} , where $H(\vec{r}) = G(\vec{r}) + V(\vec{r})$, $G(\vec{r})$ is the positive definite kinetic energy density and $V(\vec{r})$ is the potential energy density [52]. Adoption of a single QTAIM criterion for bond assessment is challenging [33]. QTAIM analyses are basis set and method independent, as long as a minimally adequate basis set is used [35]. The $\rho(\vec{r})$ and $\nabla^2\rho(\vec{r})$ topologies were performed by TOPOND, [53] which is integrated into CRYSTAL17, whereas the $\rho(\vec{r})$ topology was also performed by the Multiwfn [54] program. However, Multiwfn does not read CRYSTAL17 output files, whereas it reads output files from the GAMESS program [55]. Thus, we used the optimized geometries outputted from CRYSTAL17 as input coordinates to GAMESS, paired with the same basis sets and functionals used in CRYSTAL17. The GAMESS/Multiwfn QTAIM topological analysis is performed on a cluster extracted from the periodic layer.

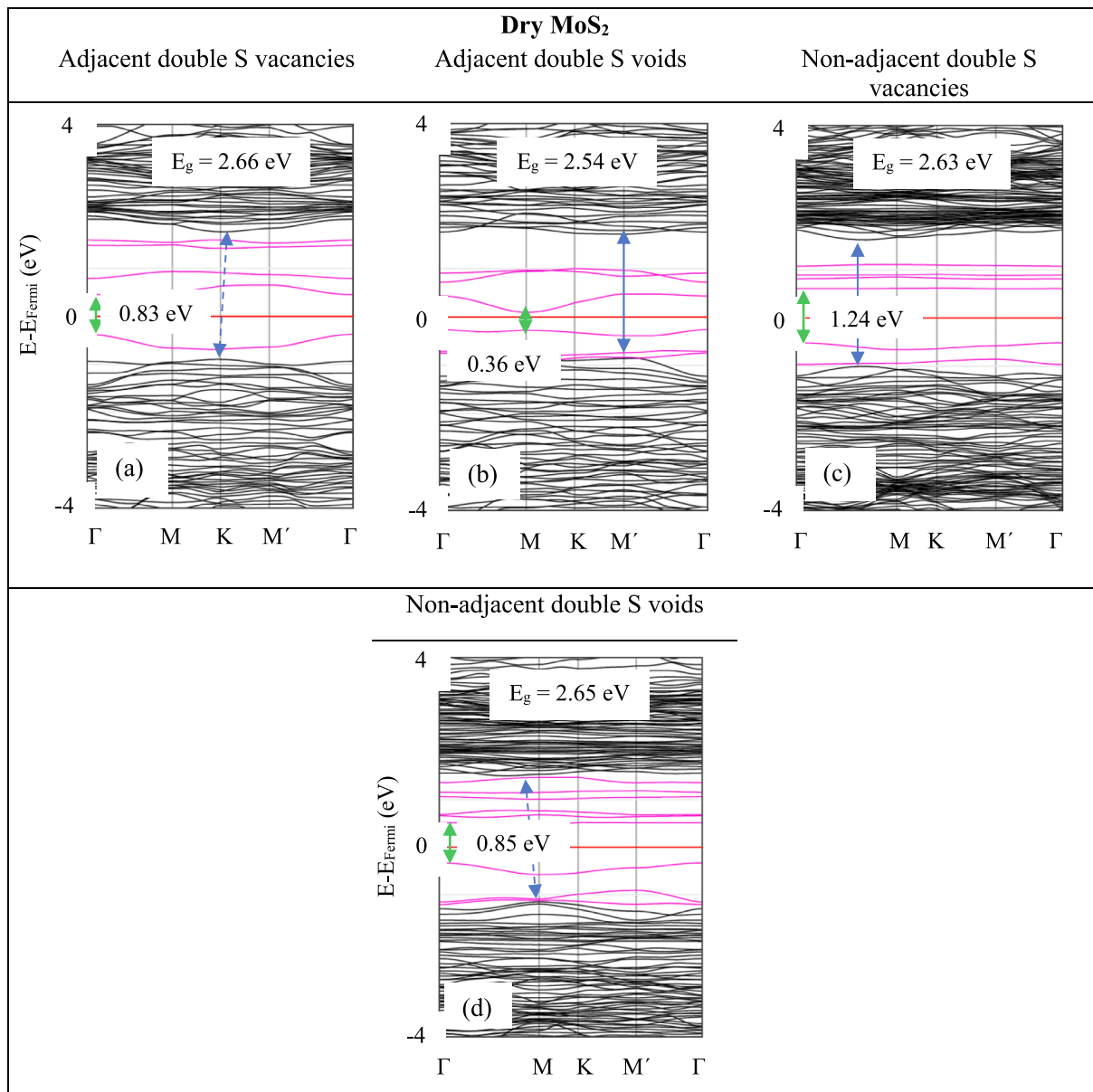


Fig. 6. (a)–(d) Band structure for the optimized geometries under the HSE06 functional for dry defect MoS_2 . Purple bands are defect bands. Blue and green arrows show bandgaps (E_g , bandgap energies) and mid-gaps, respectively. Red solid horizontal lines are the Fermi energies (E_{Fermi}). Dashed blue arrows denote indirect bandgaps. (For interpretation of the references to colour in this figure legend, the reader is referred to the web version of this article.)

3. Results and discussion

The structural parameters for pristine and defect MoS_2 have been reported previously. We found that PBE0 and HSE06 provide almost identical MoS_2 lattice parameters and geometries [5]. Water dissociation is observed during its adsorption on S voids and adjacent vacancies.

3.1. Charge redistribution due to hydration

The charge redistributions show that the adsorption of a single water molecule on pristine MoS_2 leads to small charge transfers between the water and the MoS_2 atoms, in the local area below the water molecule (Fig. 2a). Increased hydration on pristine MoS_2 causes significant charge redistribution among the water molecules, whereas minimal redistributions are observed for the support atoms. This is indicative of weak adsorption on pristine MoS_2 , in agreement with past reports [24]. However, this is in striking contrast with the cases of hydration on defect MoS_2 , where strong charge redistributions are observed in the defect

area, for all our configuration examined here (Fig. 3). These charge redistributions are maximized in the cases of adjacent double S vacancies and voids (Fig. 3c, d).

3.2. Electronic band structure and DOS analyses

Figs. 4 and 5 show the electronic band structure calculations for dry and hydrated pristine, single S vacancy, and single S void MoS_2 , using the HSE06 and PBE0 functionals. Figs. 6 and 7 show the electronic band calculations for additional dry and hydrated defect MoS_2 configurations under the HSE06 functional, whereas corresponding calculations under the PBE0 functional can be found in the supplementary material (Fig. S1 and S2). Figs. 8–10 show the DOS spectra that correspond to the pristine and defect MoS_2 configurations of this work. We observe that S vacancies introduce defect states within the electronic bandgap. Moreover, some of these defect states located around the Fermi energies, with flat band dispersion in k-space, appear as sharp peaks in the DOS.

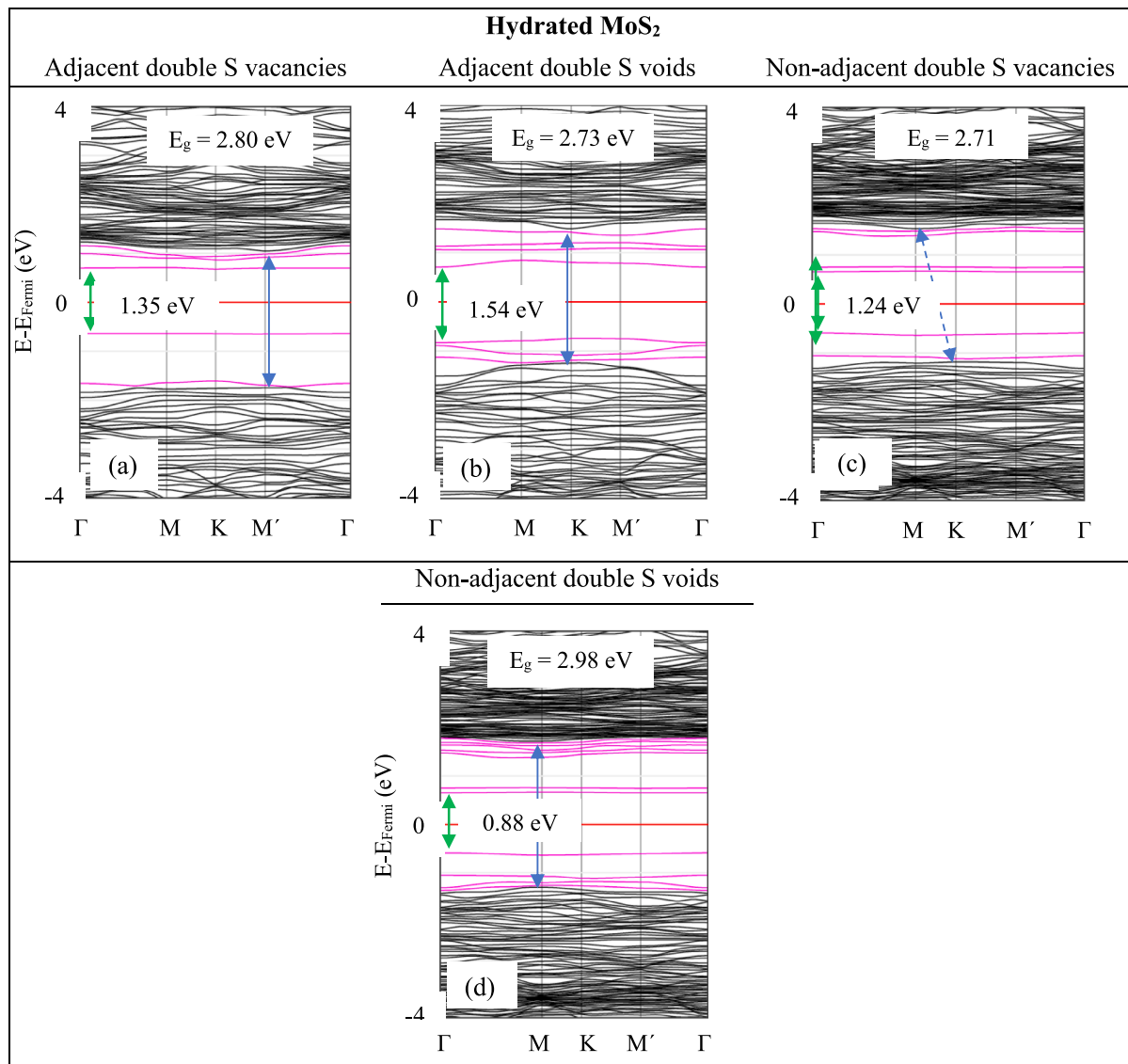


Fig. 7. (a)–(d) Band structure for the optimized geometries under the HSE06 functional for hydrated defect MoS₂. Purple bands are defect bands. Blue and green arrows show bandgaps (E_g , bandgap energies) and mid-gaps, respectively. Red solid horizontal lines are the Fermi energies (E_{Fermi}). Dashed blue arrows denote indirect band gaps. (For interpretation of the references to colour in this figure legend, the reader is referred to the web version of this article.)

3.2.1. Pristine MoS₂

Our calculations show that the pristine 2H-MoS₂ monolayer is a direct bandgap semiconductor at the K point, in agreement with past reports [17,56–59]. Our dry pristine 2H-MoS₂ calculated bandgaps are 3.19 eV and 2.54 eV, using the PBE0 and the HSE06 functionals, respectively (Fig. 4a, d). These values are larger than the experimental measured value of 1.83–1.98 eV [17,60], whereas past computational calculations reported dry pristine 2H-MoS₂ bandgaps of 1.63–2.219 eV [18,56,59]. Recently, Zhao and Lui found that the pristine MoS₂ bandgap monotonically decreases from 2.219 to 1.441 eV, as the number of layers increases from 1 to infinity [18]. Our HSE06 functional predicts MoS₂ bandgaps closer to the experimentally recorded values, whereas PBE0 functionals systematically overestimate bandgaps, for all MoS₂ configurations examined here.

Hydration minimally affects the electronic structure of the pristine MoS₂ near the Fermi energy (see Fig. 4a, d and 5a, d). The pristine MoS₂ bandgap due to hydration (0.375 ML water coverage) is increased by about 0.03 eV and 0.07 eV, for PBE0 and HSE06 calculations, respectively. Its valence and conduction bands are due to hybridization of the S-3p and Mo-4d bands (Fig. 8a). However, we must state that Mo-4d

orbitals dominate in the conduction band in agreement with past reports of Fuhr and Saúl, using local density approximation (LDA) [61] and of KC et al., using generalized gradient approximation (GGA) functionals [62].

Fig. 11 shows the highest occupied and the lowest unoccupied crystalline orbitals at the Γ point, for dry pristine and single S vacancy MoS₂. For semiconductors, the former orbitals correspond to the top of the valence bands and the latter to the bottom of the conduction bands. For the pristine case, both the highest occupied and the lowest unoccupied crystalline orbitals are predominantly due to Mo-4d_{z²} and Mo-4d_{x²-y²} orbitals, with some contribution from the sp orbitals of S, the latter due to hybridization between the S 3s and 3p orbitals (Fig. 11a, c).

3.2.2. Defect MoS₂

Defects on MoS₂ introduce direct mid-gaps [61,62], which are strongly affected by hydration (see Figs. 4–7). The number density of the mid-gaps states in the Fermi energy area depends on the defect geometry. The bandgap, defined as the energy between the top of the valence band and the bottom of the conduction band, is minimally affected by the presence of structural defects. However, hydration increases both

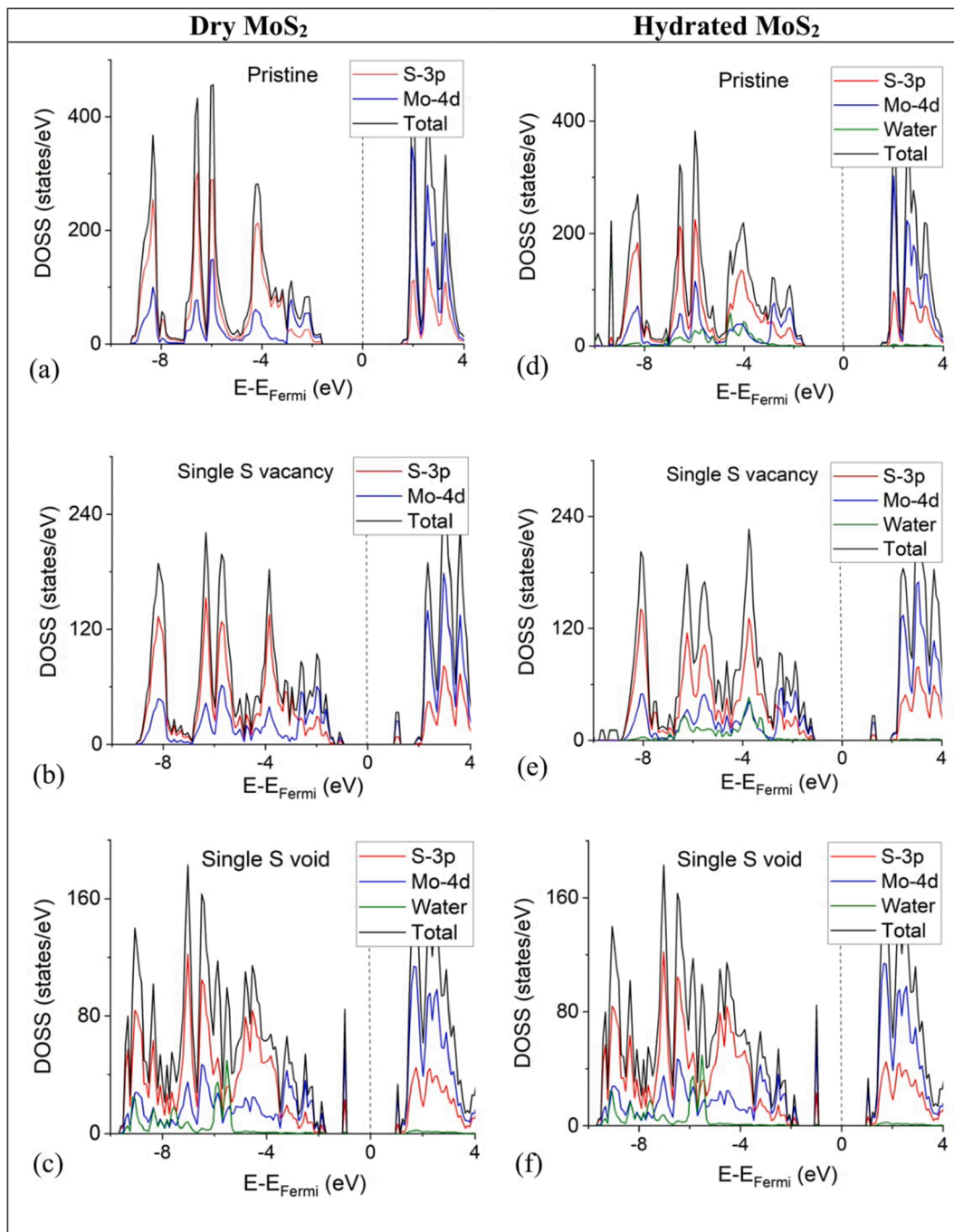


Fig. 8. DOS spectra calculated using the PBE0 functional for (a)–(c) dry defect MoS_2 per S-3p and Mo-4d orbitals and total and (d)–(f) hydrated. The dashed vertical lines are the Fermi energies (E_{Fermi}).

the bandgaps and the mid-gaps around the Fermi energy area.

Single S vacancy. The band structure calculations show that new states appear below the conduction band bottom and above the valence band top (defect states, Figs. 4b, e and 5b, e) for both dry and hydrated cases. KC et al., identified these defect states to be due to dangling Mo-4d orbitals (states below the conduction band) and decreased hybridization of S-3p and Mo-4d due to the presence of the S defect (states above the valence band) [62]. Two almost flat defect states appear below the conduction band bottom and one defect state above the valence band top. Qiu et al. [17], stated that these flat defect states above the Fermi energy are deep donor states. For dry MoS_2 , these states are degenerate, located about 0.7 eV below the conduction band bottom and separated at the K point by 0.07 eV (HSE06 calculations, Fig. 4b). Whereas for the

hydrated case, these states separate at all k-points by 0.05–0.08 eV, with the maximum separation at the K point (Fig. 5b, e). The lowest unoccupied orbital of the dry defect case, which corresponds to the deep donor flat bands, has orbital contributions mostly from Mo atoms located in the vicinity of the structural defect (corner Mo atoms, Fig. 11d). Thus, flat bands correspond to localized orbitals. However, the highest occupied orbital has contributions from both Mo atoms in the vicinity of the defect, as well as other Mo atoms (Fig. 11c). The DOS shows that the deep donor defect states have minimal contributions from the water molecules orbitals. This could be associated with the fact that water molecules do not dissociate on the defect site of the single S vacancy. However, water dissociation could substantially alter these defect states upon hydration (vide infra).

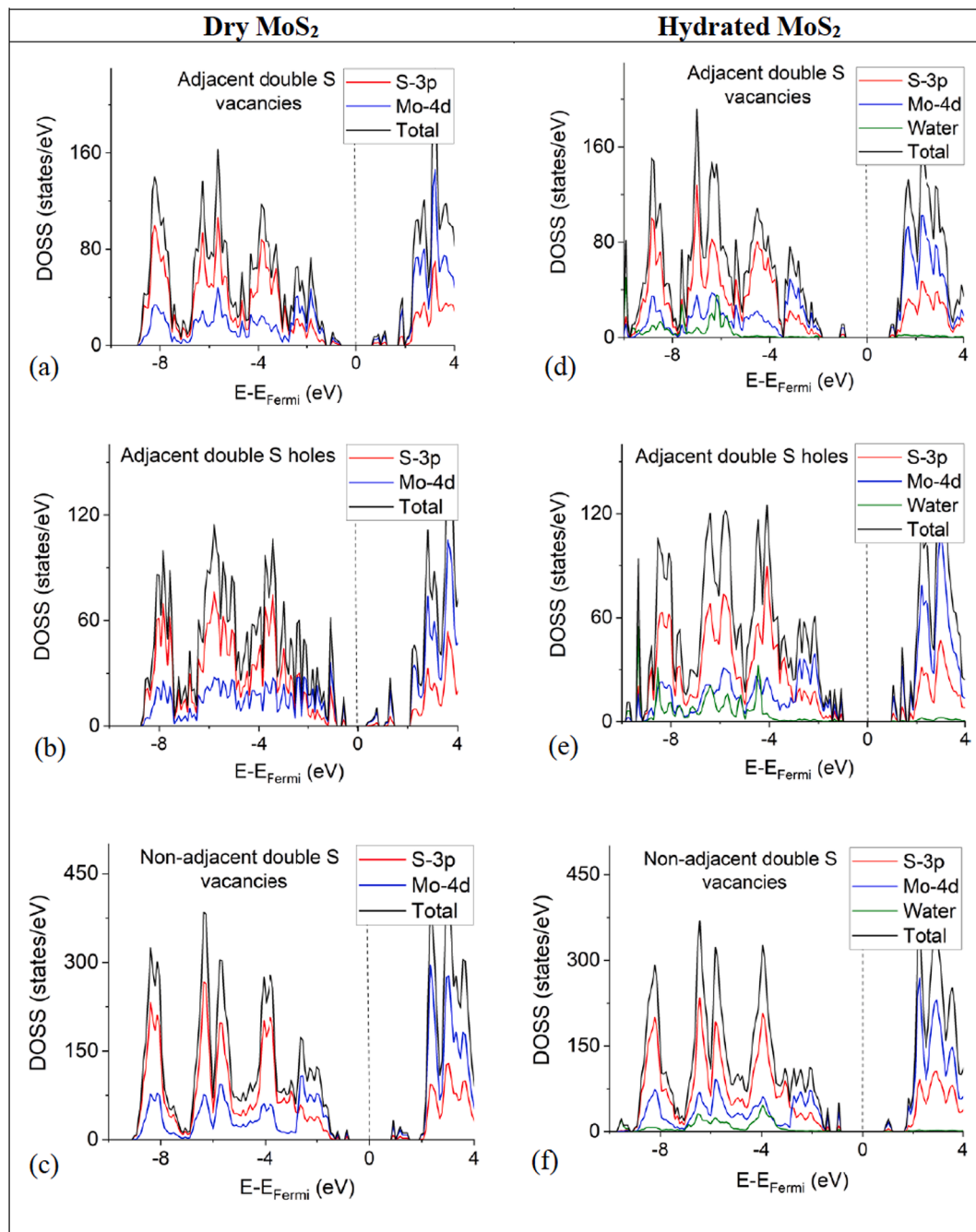


Fig. 9. DOS spectra calculated using the PBE0 functional for (a)–(c) dry defect MoS_2 per S-3p and Mo-4d orbitals and total and (d)–(f) hydrated. The dashed vertical lines are the Fermi energies (E_{Fermi}).

Single S void. The presence of an additional S vacancy at the bottom MoS_2 layer forming a void is associated with additional defect states relative to the single S vacancy configuration, for both dry and hydrated cases. We observe differences in the bands structure between M and \bar{M} points, which is indicative of broken symmetry. This effect is also observed for all remaining defect MoS_2 configurations examined in this work. For the dry MoS_2 configuration, two additional defect states appear in the band structure and overlap with the conduction band bottom at the K point. In this case, the energy separation of the degenerate deep donor bands at the K point is increased to 0.15 eV (HSE06 calculations). However, upon hydration, one of these two defect states is pushed below the Fermi energy and appears as a sharp peak in the DOS (Fig. 8f). This sticking difference in the MoS_2 band structure is due to water dissociation in the area of the S void, which is also observed to all

remaining hydrated defect MoS_2 examined here. This dissociation causes OH adsorption on Mo atoms at the void site, whereas the remaining hydrogen from the dissociated water molecule resides away from the void. The mid-gap here is smaller than the one observed for the single S vacancy MoS_2 .

Adjacent double S vacancies and voids. In these cases, several defect bands appear above and below the Fermi energy in the bandgap region. For the adjacent double S vacancies dry MoS_2 configurations, the bandgap is indirect between the K point in the valence band top and a point between K and \bar{M} in the conduction band bottom. However, for the corresponding adjacent double S void case, the bandgap is direct at the M point.

We now compare the band structure of the single S vacancy with the adjacent double S vacancies (Fig. 4b, e and 6a). For the dry

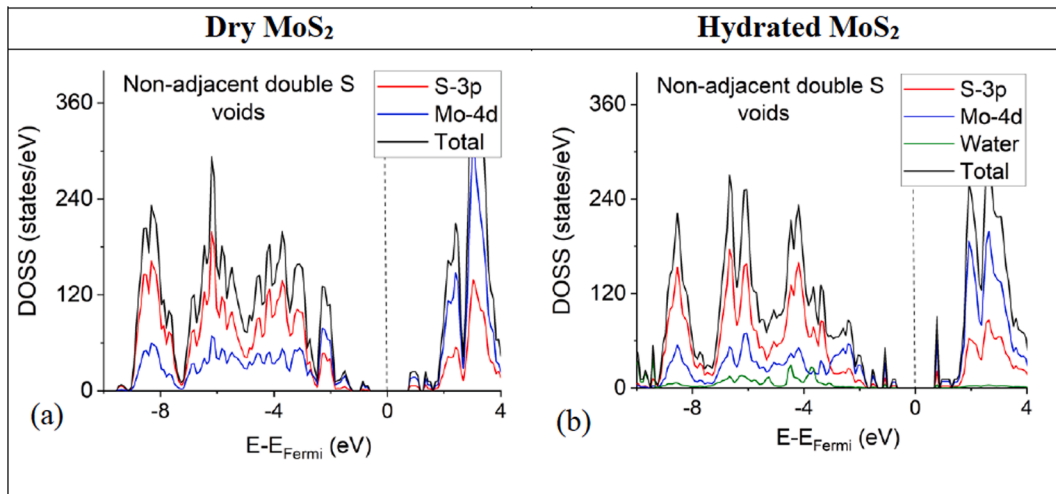


Fig. 11. Crystalline orbitals calculated from CRYSTAL17 under the PBE0 functional (a) highest occupied orbital for dry pristine MoS_2 , (b) its lowest unoccupied orbital, (c) highest occupied orbital for dry single S void vacancy MoS_2 , and (d) its lowest unoccupied orbital. Atoms colors are as follows: S yellow; Mo, green. (For interpretation of the references to colour in this figure legend, the reader is referred to the web version of this article.)

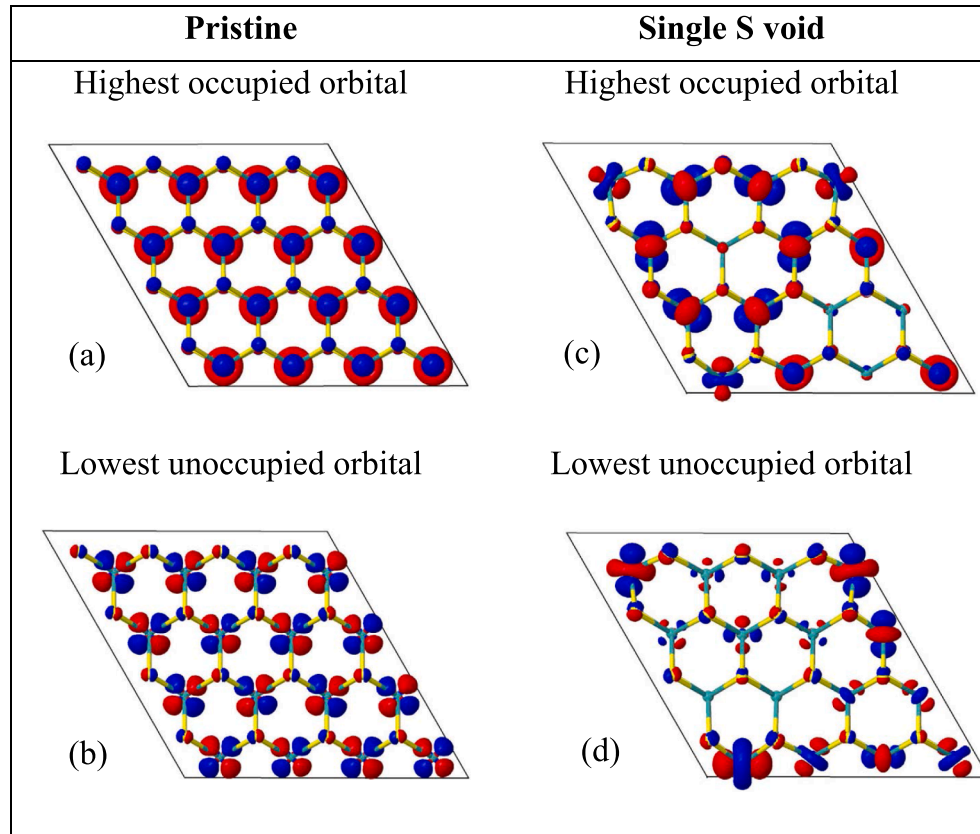


Fig. 12. QTAIM molecular graphs obtained from the DFT optimized unit cell for dry MoS_2 , using Multiwfn and plotted via VMD [67]. Small and large spheres denote critical points and atoms, respectively. (a) oblique, (b) side, and (c) focused top views. Atoms are colors as follows: S, yellow; Mo, green; O, red; H, white. QTAIM critical points are colors as follows: (3, -3), purple; (3, -1), blue; (3, +1), gray; (3, +3), green. Additional (3, +3) critical points of low ρ located at 0.05 Å above the Mo atoms are not shown. (For interpretation of the references to colour in this figure legend, the reader is referred to the web version of this article.)

configurations, the addition of the second vacancy introduces two more defect states between the Fermi energy and the conduction band bottom. Moreover, the defect state just above the valence band top is now pushed closer to the Fermi energy relative to the single S vacancy configuration. Here, the defect states between the Fermi energy and the conduction band bottom of the dry configurations are as not flat as in the single S vacancy case. However, hydration, associated with OH adsorption, introduces flat-type bands below the conduction band and above the valence band, and thus orbital localizations around the defects. This effect is also evidenced for the hydrated adjacent double voids

configuration.

The band structures and the DOS between the single and adjacent double voids are stinkingly different. In a similar fashion as the adjacent double S vacancy discussed above, the second void also introduces more defect states in the Fermi energy area. We observe that for the dry configuration, the defect states that overlapped at the K point with the conduction band bottom in the single void case are now pushed closer to the Fermi energy in the adjacent double void. Here, the mid-gap at the dry adjacent double void configuration is the smallest observed (i.e., 0.36 eV, see Fig. 6b) in this work. Recall that smaller bandgaps and mid-

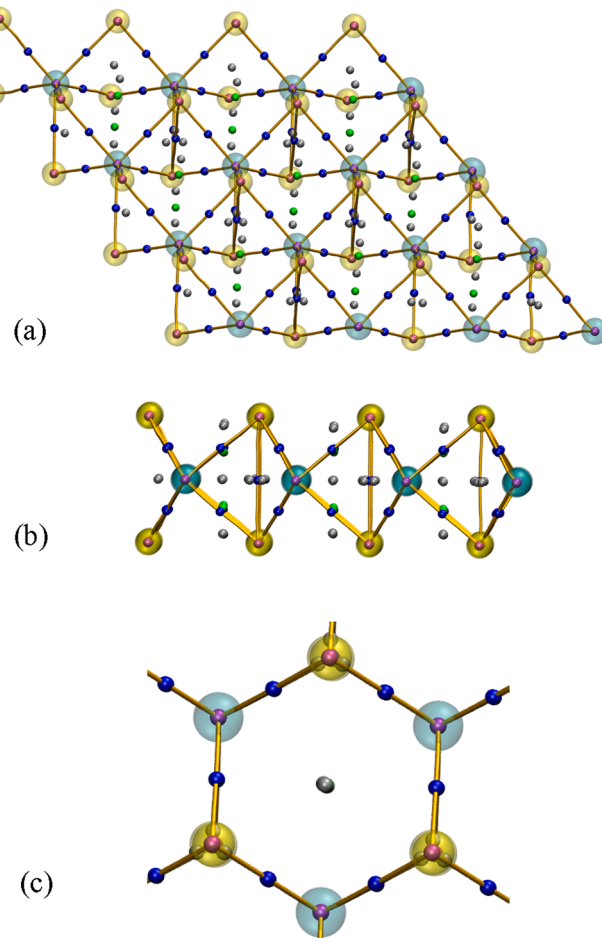


Fig. 13. The negative of the Laplacian $-\nabla^2\rho$ distribution for dry pristine MoS_2 (a) along the bond path S-Mo and (b) S-S and in the plane defined by (c) the top layer S atoms and (d) two Mo atoms and one S top layer atom, showing the side of the MoS_2 . Dashed curve in (a) denotes calculations with density matrix obtained by superposition of atomic densities. Blue and red denote low and high charge concentrations, respectively. The Mo core is described by a pseudopotential.

gaps lead to increased electron conductivity, and thus making this material a good candidate for electrocatalysis, especially, for HER. However, its effectiveness as HER catalyst upon hydration significantly decreases since its mid-gap increases upon hydration (i.e., 1.54 eV, see Fig. 7b).

Non-adjacent double S vacancies and voids. There are some major differences in the band structure of the MoS_2 configurations with adjacent double S vacancies to those where vacancies are further apart (e.g., non-adjacent double S vacancies). This statement is also valid for double S voids. For example, when the two S vacancies and not adjacent to each other, the defect bands in the area between the Fermi energy and the conduction band bottom are flat, for both dry and hydrated configurations (Figs. 6c and 7c). For non-adjacent S voids, hydration flattens the defect states in the area between the Fermi energy and the valence band top. The calculated bandgaps for the dry configuration of the non-adjacent double S vacancies and the hydrated configuration for non-adjacent double voids are direct, whereas the opposite is observed for the other two configurations examined in this subsection. It is observed that the dry MoS_2 configurations with non-adjacent double S voids has the second smaller mid-gap reported here (0.85 eV; Fig. 6d). In contrast to the configuration of the adjacent double S voids discussed above, hydration minimally affects the mid-gap of the non-adjacent double S voids configurations. Therefore, MoS_2 monolayer with adjacent double S voids serves better for HER electrocatalysis under both dry

and hydrated conditions.

3.3. QTAIM calculations

3.3.1. The Mo—S and S—S bonding

Fig. 12 shows the QTAIM molecular graphs and the (3, -3), (3, -1), (3, +1), and (3, +3) critical points for the dry pristine MoS_2 , as calculated by the Multiwfnn program. Additional calculations using the TOPOND program will reveal low $\rho(\vec{r})$ (3, +3) points of about 1.35×10^{-3} a. u. located at 0.05 Å from the Mo atoms and towards the MoS_2 surface. The importance of these points will be discussed in the next subsection. The QTAIM molecular graph, which provides information on bonding, is a collection of bond paths linking the nuclei of bonded atoms (i.e., (3, -3) critical points) with the associated bond critical points (i.e., (3, -1) critical points) [63]. The molecular graph shows Mo—S and S—S bonding only, which is in agreement with past reports for MoS_2 bulk [64] and monolayers [36]. For the S—S bonding, the S atoms belong to different layers and are opposite to each other.

The Mo—S and S—S bonding type is identified via the QTAIM calculated properties at the corresponding bond critical points. We will classify the above bonding types using both the Espinosa et al. [65] and the Macchi et al. [66] classifications. The Espinosa et al. approach classifies bonds based on the value of the $(|V|/G)(\vec{r})$ ratio, at the bond critical points. For closed shell interactions $(|V|/G)(\vec{r}) > 1$, whereas $(|V|/G)(\vec{r}) < 1$ is expected for open shell interactions, such as covalent bonding. Values $1 < (|V|/G)(\vec{r}) < 2$ refer to the transit region, where there is an incipient covalent bond formation. Table 1 shows several QTAIM properties at Mo-S bond critical points and their corresponding Mo-S distances, for all configurations studied here. For the defect configurations we report QTAIM information, which correspond to the shortest Mo-S distance and is found in the local area of the defects. The QTAIM properties for the S-S bonding for pristine MoS_2 are found in the Table S1 (supplementary material). Here, the $(|V|/G)(\vec{r})$ values, at the Mo-S and S-S bond critical points, are 1.68–1.71 and 1, respectively. Thus, under the Espinosa et al. approach, both Mo—S and S—S bonding interactions are in the transient region, with the latter being on the border between the closed shell and the transit region. In the transient region, $H(\vec{r}) < 0$ and $\nabla^2\rho(\vec{r}) > 0$ at bond critical points, in agreement with our results (Tables 1 & S1). The Mo—S bonding is stronger than the S—S bonding, due to the significantly larger electron density and $(H/\rho)(\vec{r})$ at the corresponding bond critical points.

For bonding that involves heavy atoms, Macchi et al., used the $-\nabla^2\rho(\vec{r})$ distribution along the bond path and the delocalization index δ , as additional tools for bonding type classification. The delocalization indices for Mo—S and S—S bonding interactions for dry pristine MoS_2 were calculated from the Multiwfnn program. Macchi et al. emphasized that for these interactions their bonding classifications cannot be solely based on the sign of the Laplacian $\nabla^2\rho(\vec{r})$, at the bond critical points. Fig. 13a, b shows the $-\nabla^2\rho(\vec{r})$ distribution for dry pristine MoS_2 along the bond paths S—Mo and S—S and several in-plane contour maps. For both cases, the bond critical points are inside a flat region along the bond path, which is could be interpreted as closed shell interactions. We also calculate $-\nabla^2\rho(\vec{r})$ distributions for the above bonds, where the density matrix was obtained by superposition of atomic densities. Fig. 13a, b shows that the $-\nabla^2\rho(\vec{r})$ distributions between calculations using the periodic wavefunction and superpositions of atomic densities only differ slightly in the area of the Mo atom.

Macchi et al. states that closed and open shell interactions are expected to have, at bond critical points, $(H/\rho)(\vec{r}) > 0$, $(G/\rho)(\vec{r}) > 1$, and $\delta \approx 0$ and $(H/\rho)(\vec{r}) < 0$, $(G/\rho)(\vec{r}) < 1$, and δ approximately equal or less than the formal bond order, respectively. The in-plane contour maps show that the $-\nabla^2\rho(\vec{r})$ distribution is atom-like, with some polarization in the Mo shells. At the Mo—S bond critical points, $(H/\rho)(\vec{r}) < 0$,

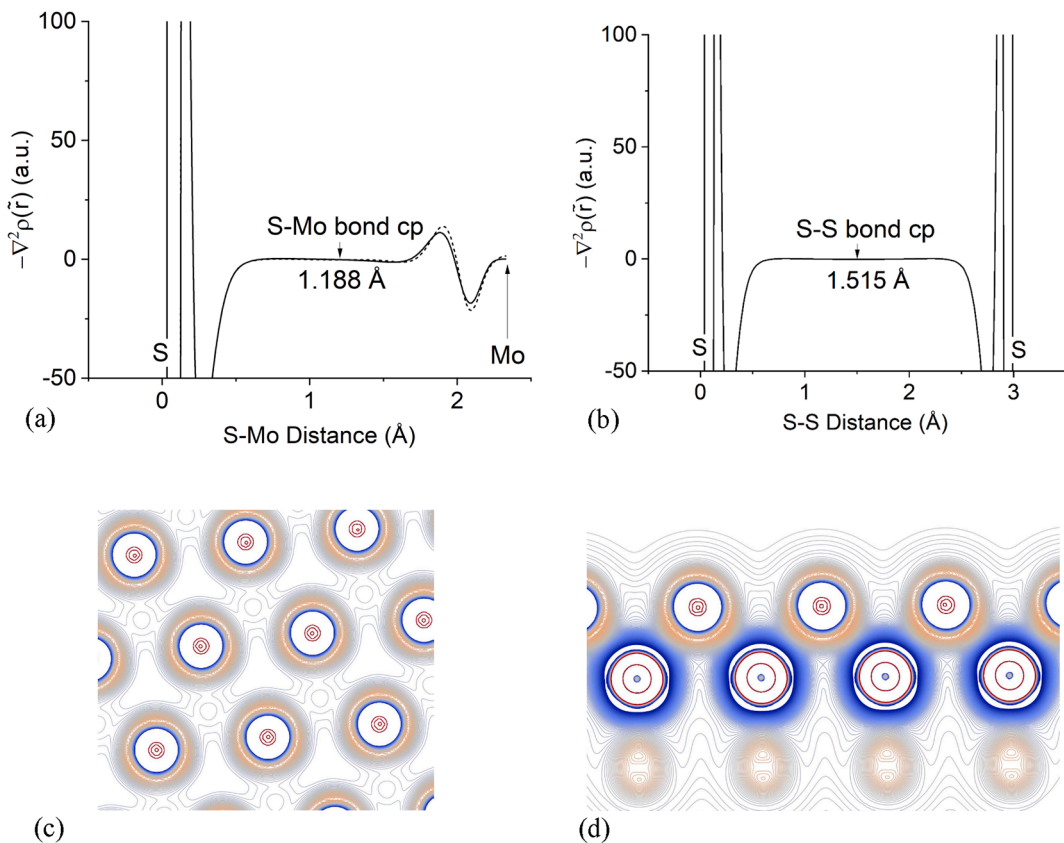


Fig. 14. Electron density ρ at Mo–S bond critical points (bcps) vs. mid-gaps for (a) dry and hydrated MoS_2 with voids and (b) with S vacancies. The linear fits and the R^2 values are shown. For comparison, we also include calculations using the pristine MoS_2 (dry and hydrated). For the defect MoS_2 configurations, the Mo–S bcp correspond to the smallest of the Mo–S distances. For pristine MoS_2 , the mid-gap is the bandgap.

Table 1

Mo–S distances and TOPOND calculated QTAIM parameters $\rho(\vec{r}_{bcp})$, $\nabla^2\rho(\vec{r}_{bcp})$, $(H/\rho)(\vec{r}_{bcp})$ and $(G/\rho)(\vec{r}_{bcp})$ at bond critical points (bcps) for dry pristine and defect MoS_2 . Values in parentheses refer to the corresponding hydrated cases. For the defect MoS_2 , the parameters that correspond to the smaller Mo–S are reported. For the hydrated pristine MoS_2 configuration, the Mo–S distance refer to a top layer S atom located at about 2.8 Å relative to a water molecule.

MoS_2	Distances (Å)	QTAIM properties (a.u.)			
		$\rho(\vec{r}_{bcp})$	$\nabla^2\rho(\vec{r}_{bcp})$	(H/ρ)	(G/ρ)
		(\vec{r}_{bcp})		(\vec{r}_{bcp})	
Pristine	2.33 (2.31)	0.108 (0.110)	0.137 (0.143)	−0.454 (−0.462)	0.771 (0.787)
Single S vacancy	2.26 (2.27)	0.125 (0.120)	0.132 (0.137)	−0.534 (−0.511)	0.799 (0.796)
Single S void	2.32 (2.29)	0.113 (0.114)	0.113 (0.168)	−0.487 (−0.480)	0.738 (0.847)
Adjacent 2 S vacancies	2.25 (2.26)	0.127 (0.120)	0.111 (0.137)	−0.549 (−0.511)	0.767 (0.796)
Adjacent 2 S voids	2.29 (2.22)	0.118 (0.133)	0.128 (0.134)	−0.502 (−0.564)	0.774 (0.818)
Non-adjacent 2 S vacancies	2.26 (2.28)	0.124 (0.118)	0.133 (0.149)	−0.532 (−0.498)	0.799 (0.815)
Non-adjacent 2 S voids	2.27 (2.29)	0.122 (0.115)	0.112 (0.149)	−0.526 (−0.484)	0.756 (0.806)

$(G/\rho)(\vec{r}) \approx 0.74\text{--}0.85$, and $\delta \approx 1$, the latter being equal to the formal Mo–S bond order. Thus, Mo–S bond is weakly polar covalent ($\nabla^2\rho > 0$) since ρ at the Mo–S bond critical points is small. At the S–S bond critical points, $H \approx 0$, $G/\rho = 1$, and $\delta \approx 0$, which agree that S–S interaction is of a closed shell.

3.3.2. Water interaction on MoS_2

Water adsorption on pristine MoS_2 is weak. However, water and its dissociated components OH and H are strongly adsorbed on S defects and voids, by bonding on the Mo sites in the areas of the S defects [5]. In these cases, the Mo sites are accessible to the adsorbates since they are not blocked by S atoms, in agreement with previous reports [36]. Water, H, and OH bind at the Mo atoms in a form of an electrophile–nucleophile interaction. These and other adsorbents seek points of least $\rho(\vec{r})$ on MoS_2 , which act as a Lewis acid sites. These points are (3, +3) critical points. For the (3, +3) critical points shown in Fig. 12, their $\rho(\vec{r})$ values are 1.22×10^{-2} a.u. and about 1.31×10^{-2} a.u. for pristine and void defect, respectively. These points are located above and below the Mo plane. However, there are additional (3, +3) critical points of substantially lower $\rho(\vec{r})$ values ($\sim 1.31 \times 10^{-3}$ a.u.) located 0.05 Å above the Mo atoms and are resolved by TOPOND. The presence of S vacancies and voids allow these points to be accessible to adsorbates.

3.3.3. Correlation between mid-gap energies and electron density at bond critical points

Fig. 14 shows negative correlations between the $\rho(\vec{r})$ values at the Mo–S bond critical points of the shortest Mo–S distance and the mid-gap in the Fermi energy area, for dry and hydrated MoS_2 defect configurations. The rational is that since mid-gaps are due to structural defects, they should be correlated with QTAIM properties at critical points in the

area of the defect. We found that we can obtain improved correlations if we treat S vacancies and voids separately (Fig. 14a & b).

Larger $\rho(\vec{r})$ values at the Mo—S bond critical points belong to MoS₂ configurations with smaller mid-gaps. Recall that for MoS₂ defect configurations the shortest Mo—S are observed in the area of the structural defect. Table 1 shows that larger $\rho(\vec{r})$ values are also associated with larger $(H/\rho)(\vec{r})$ values, which is indicative of more covalent Mo—S bonding at the area of the defect. As discussed above, smaller mid-gaps are associated with higher conductivity. Therefore, higher conductivity for MoS₂ is associated with the Mo-S bonding being more covalent in the area of the defect.

4. Conclusions

In summary, periodic DFT electronic band structure calculations on 2H-MoS₂ monolayers show that structural S defects introduce defect bands and mid-gaps within the bandgap, in the vicinity of the Fermi energy. Hydration affects the defect MoS₂ electronic band structure, by shifting the defect bands and changing the mid-gaps. QTAIM calculations show that only Mo—S and S—S bonding are available in the MoS₂ monolayers, the former being weakly covalent and the latter of a closed shell interaction. Water molecules and their dissociated constituents H and OH are strongly adsorbed on the Mo sites, only when S defects are available. This is due to the presence of low electron density regions, which are located very close to the Mo sites and are required for nucleophiles to bind. Finally, we observed a negative correlation between electron density at Mo—S bond critical points around the structural defect and the defect MoS₂ mid-gap. Defects associated with higher $\rho(\vec{r})$ at Mo-S bond critical points in the area of the defect introduce smaller mid-gaps, which in turn increase the MoS₂ conductivity thus, assisting in accelerating the HER during electrocatalysis for hydrogen fuel economy.

CRediT authorship contribution statement

Nicholas Dimakis: Conceptualization, Methodology, Formal analysis, Supervision, Project administration, Writing - review & editing. **Om Vadodaria:** Investigation, Data curation, Writing - original draft. **Korinna Ruiz:** Investigation, Data curation, Writing - original draft. **Sanju Gupta:** Conceptualization, Methodology, Formal analysis, Writing - review & editing.

Declaration of Competing Interest

The authors declare that they have no known competing financial interests or personal relationships that could have appeared to influence the work reported in this paper.

Appendix A. Supplementary material

Supplementary data to this article can be found online at <https://doi.org/10.1016/j.apsusc.2021.149545>.

References

- [1] R.G. Dickinson, L. Pauling, The crystal structure of molybdenite, *J. Am. Chem. Soc.* 45 (1923) 1466–1471.
- [2] M.V. Bollinger, K.W. Jacobsen, J.K. Nørskov, Atomic and electronic structure of MoS₂ nanoparticles, *Phys. Rev. B* 67 (2003) 085410–085417.
- [3] Q. Peng, S. De, Outstanding mechanical properties of monolayer MoS₂ and its application in elastic energy storage, *Phys. Chem. Chem. Phys.* 15 (2013) 9427–19437.
- [4] D. Gao, M. Si, J. Li, J. Zhang, Z. Zhang, Z. Yang, D. Xue, Ferromagnetism in freestanding MoS₂ nanosheets, *Nanoscale Res. Lett.* 8 (2013) 129–1128.
- [5] S. Gupta, T. Robinson, N. Dimakis, Electrochemically desulfurized molybdenum disulfide (MoS₂) and reduced graphene oxide aerogel composites as efficient electrocatalysts for hydrogen evolution, *J. Nanosci. Nanotechnol.* 20 (2020) 6191–6214.
- [6] B. Hinnemann, P.G. Moses, J. Bonde, K.P. Jørgensen, J.H. Nielsen, S. Horch, I. Chorkendorff, K.J. Nørskov, Biomimetic hydrogen evolution: MoS₂ nanoparticles as catalyst for hydrogen evolution, *J. Am. Chem. Soc.* 127 (2005) 5308–5309.
- [7] A. Fujishima, K. Honda, Electrochemical photolysis of water at a semiconductor electrode, *Nature* 238 (1972) 37–58.
- [8] R.S. Trasatti, Work function, electronegativity, and electrochemical behaviour of metals: III. Electrolytic hydrogen evolution in acid solutions, *J. Electroanal. Chem.* 39 (1972) 163–184.
- [9] N. Kumar, J.M. Seminario, Computational chemistry analysis of hydrodesulfurization reactions catalyzed by molybdenum disulfide nanoparticles, *Phys. Chem. C* 119 (2015) 29157–29170.
- [10] M. Chhowalla, G. Amaralatunga, Thin films of fullerene-like MoS₂ nanoparticles with ultra-low friction and wear, *Nature* 407 (2000) 164–167.
- [11] M.R. Vazirisereshk, A. Martini, D.A. Strubbe, M.Z. Baykara, Solid lubrication with MoS₂: a review, *Lubricants* 7 (2019) 57–135.
- [12] S. Domínguez-Meister, T.C. Rojas, M. Brizuela, J.C. Sánchez-López, Solid lubricant behavior of MoS₂ and WSe₂-based nanocomposite coatings, *Sci. Technol. Adv. Mater.* 18 (2017) 122–133.
- [13] L. Rapoport, N. Fleischerb, R. Tenne, Applications of WS₂ (MoS₂) inorganic nanotubes and fullerene-like nanoparticles for solid lubrication and for structural nanocomposites, *J. Mater. Chem.* 15 (2005) 1782–1788.
- [14] K.S. Novoselov, D. Jiang, F. Schedin, T.J. Booth, V.V. Khotkevich, S.V. Morozov, A. K. Geim, Two-dimensional atomic crystals, *Proc. Natl. Acad. Sci. U. S. A.* 102 (2005) 10451–10453.
- [15] G. Eda, H. Yamaguchi, D. Voiry, T. Fujita, C. M., M. Chhowalla, Photoluminescence from chemically exfoliated MoS₂, *Nano Lett.* 11 (2011) 5111–5116.
- [16] B. Han, Y.H. Hu, MoS₂ as a co-catalyst for photocatalytic hydrogen production from water, *Energy Sci. Eng.* 4 (2016) 285–304.
- [17] K.F. Mak, C. Lee, J. Hone, J. Shan, T.F. Heinz, Atomically thin MoS₂: a new direct-gap semiconductor, *Phys. Rev. Lett.* 105 (2010) 136805–1136804.
- [18] Z.-Y. Zhao, Q.-L. Liu, Study of the layer-dependent properties of MoS₂ nanosheets with different crystal structures by DFT calculations, *Catal. Sci. Technol.* 8 (2018) 1867–1879.
- [19] T.F. Jaramillo, K.P. Jørgensen, J. Bonde, J.H. Nielsen, S. Horch, I. Chorkendorff, Identification of active edge sites for electrochemical H₂ evolution from MoS₂ nanocatalysts, *Science* 317 (2007) 100–102.
- [20] Y. Cheng, H. Song, H. Wu, P. Zhang, Z. Tang, S. Lu, Defects enhance the electrocatalytic hydrogen evolution properties of MoS₂-based materials, *Chem. Asian J.* 15 (2020) 3123–3134.
- [21] X.-L. Fan, Y. Yang, P. Xiao, W.-M. Lau, Site-specific catalytic activity in exfoliated MoS₂ single-layer polytypes for hydrogen evolution: basal plane and edges, *J. Mater. Chem. A* 2 (2014) 20545–20551.
- [22] E.S. Kadantsev, P. Hawrylak, Electronic structure of a single MoS₂ monolayer, *Solid State Commun.* 152 (2012) 909–913.
- [23] H. Qiu, T. Xu, Z. Wang, W. Ren, H. Nan, Z. Ni, Q. Chen, S. Yuan, F. Miao, F. Song, G. Long, Y. Shi, L. Sun, J. Wang, X. Wang, Hopping transport through defect-induced localized states in molybdenum disulphide, *Nat. Commun.* 4 (2013) 2642–2646.
- [24] B. Zhao, C. Shang, N. Qi, Z.Y. Chen, Z.Q. Chen, Stability of defects in monolayer MoS₂ and their interaction with O₂ molecule: A first-principles study, *Appl. Surf. Sci.* 412 (2017) 385–393.
- [25] J. Hong, Z. Hu, M. Probert, K. Li, D. Lv, X. Yang, L. Gu, N. Mao, Q. Feng, L. Xie, J. Zhang, D. Wu, Z. Zhang, C. Jin, W. Ji, X. Zhang, J. Yuan, Z. Zhang, Exploring atomic defects in molybdenum disulphide monolayers, *Nat. Commun.* 6 (2015) 6293–6298.
- [26] T. Li, G. Galli, Electronic properties of MoS₂ nanoparticles, *J. Phys. Chem. C* 111 (2007) 16192–16196.
- [27] J.K. Ellis, M.J. Lucero, G.E. Scuseria, The indirect to direct band gap transition in multilayered MoS₂ as predicted by screened hybrid density functional theory, *Appl. Phys. Lett.* 99 (2011) 261908–1261903.
- [28] S.W. Han, G.-B. Cha, K. Kim, S.C. Hong, Hydrogen interaction with a sulfur-vacancy-induced occupied defect state in the electronic band structure of MoS₂, *Phys. Chem. Chem. Phys.* 21 (2019) 15302–15309.
- [29] W. He, J. Shi, H. Zhao, H. Wang, X. Liu, X. Shi, Bandgap engineering of few-layered MoS₂ with low concentrations of S vacancies, *RSC Adv.* 10 (2020) 15702–15706.
- [30] H. Li, C. Tsai, A.L. Koh, L. Cai, A.W. Contriman, A.H. Fragapane, J. Zhao, H.S. Han, H.C. Manoharan, F. Abild-Pedersen, J.K. Nørskov, X. Zheng, Activating and optimizing MoS₂ basal planes for hydrogen evolution through the formation of strained sulphur vacancies, *Nature Mater.* 15 (2016) 48–53.
- [31] R. Bader, *Atoms in Molecules: A Quantum Theory*, Oxford Univ. Press, Oxford, 1990.
- [32] R.F.W. Bader, *Atoms in Molecules. Encyclopedia of Computational Chemistry*, John Wiley and Sons, 1998.
- [33] C. Gatti, Chemical bonding in crystals: new directions, *Z. Kristallogr. Cryst. Mater.* 220 (2005) 399–457.
- [34] R.F.W. Bader, A bond path: A universal indicator of bonded interactions, *J. Phys. Chem. A* 102 (1998) 7314–7323.
- [35] M. Jablonski, M. Palusiak, Basis set and method dependence in atoms in molecules calculations, *J. Phys. Chem. A* 114 (2010) 2240–2244.
- [36] Y. Aray, J. Rodriguez, Atoms in molecules theory for exploring the nature of the MoS₂ catalyst edges sites, *J. Mol. Catal. A Chem.* 265 (2007) 32–41.
- [37] Y. Aray, Exploring the electron density localization in single MoS₂ monolayers by means of a localized-electrons detector and the quantum theory of atoms in molecules, *AIP Adv.* 7 (2017) 115106–115110.
- [38] Y. Aray, A.D. Barrios, Exploring the electron density localization in MoS₂ nanoparticles using a localized-electron detector: Unraveling the origin of the one-

dimensional metallic sites on MoS₂ catalysts, *Phys. Chem. Chem. Phys.* 20 (2018) 20417–20426.

[39] M.A. Syzgantseva, O.A. Syzgantseva, QTAIM method for accelerated prediction of band gaps in perovskites, *Theor. Chem. Acc.* 138 (2019) 52–58.

[40] N. Seriani, A relation between kinetic-energy density and the band gap in alkali and alkaline-earth oxides, *J. Phys. Condens. Matter* 22 (2010) 255502–255505.

[41] C.J. Kang, Correlation of bond metallicity measures to electronegativity for binary oxides, *Int. J. Quantum Chem.* 118 (2018), 25548–25512.

[42] K. Momma, F. Izumi, VESTA 3 for three-dimensional visualization of crystal, volumetric and morphology data, *J. Appl. Crystallogr.* 44 (2011) 1272–1276.

[43] R. Dovesi, V.R. Saunders, C. Roetti, C.M. Zicovich-Wilson, F. Pascale, B. Civalleri, K. Doll, N.M. Harrison, I.J. Bush, P. D'Arco, M. Llunell, M. Causà, Y. Noël, L. Maschio, R. Orlando, A. Erba, M. Rérat, S. Casassa, CRYSTAL17 User's Manual, Univ. Torino, Torino, 2017.

[44] M. Ernzerhof, G.E. Scuseria, Assessment of the Perdew–Burke–Ernzerhof exchange–correlation functional, *J. Chem. Phys.* 110 (1999) 5029–5036.

[45] C. Adamo, V. Barone, Toward reliable density functional methods without adjustable parameters: The PBE0 model, *J. Chem. Phys.* 110 (1999) 6158–6170.

[46] A.V. Kruckau, O.A. Vydróv, A.F. Izmaylov, G.E. Scuseria, Influence of the exchange screening parameter on the performance of screened hybrid functionals, *J. Chem. Phys.* 125 (2006), 224106–224105.

[47] S. Grimme, J. Antony, S. Ehrlich, H. Krieg, A consistent and accurate ab initio parametrization of density functional dispersion correction (DFT-D) for the 94 elements H–Pu, *J. Chem. Phys.* 132 (2010) 154104–154118.

[48] M.F. Peintinger, D.V. Oliveira, T. Bredow, Consistent Gaussian basis sets of triple-zeta valence with polarization quality for solid-state calculations, *J. Comput. Chem.* 34 (2013) 451–459.

[49] A. Mahmoud, A. Erba, K.E. El-Kelany, M. Rérat, R. Orlando, Low-temperature phase of BaTiO₃: Piezoelectric, dielectric, elastic, and photoelastic properties from *ab initio* simulations, *Phys. Rev. B* 89 (2014) 045103–045109.

[50] J. Laun, D.V. Oliveira, T. Bredow, Consistent gaussian basis sets of double- and triple-zeta valence with polarization quality of the fifth period for solid-state calculations, *J. Comput. Chem.* 39 (2018) 1285–1290.

[51] H.J. Monkhorst, J.D. Pack, Special points for Brillouin-zone integrations, *Phys. Rev. B* 13 (1976) 5188–5192.

[52] P. Macchi, D.M. Proserpio, A. Sironi, Experimental electron density in a transition metal dimer: metal–metal and metal–ligand bonds, *J. Am. Chem. Soc.* 120 (1998) 13429–13435.

[53] C. Gatti, TOPOND-96 : an electron density topological program for systems periodic in N (N=0–3) dimensions, User's manual, CNR-CSRSRC, Milano (1996).

[54] T. Lu, F. Chen, Multiwfns: A multifunctional wavefunction analyzer, *J. Comput. Chem.* 33 (2012) 580–592.

[55] M.W. Schmidt, K.K. Baldridge, J.A. Boatz, S.T. Elbert, M.S. Gordon, J.H. Jensen, S. Koseki, N. Matsunaga, K.A. Nguyen, S. Su, T.L. Windus, M. Dupuis, J. A. Montgomery, General atomic and molecular electronic structure system, *J. Comput. Chem.* 14 (1993) 1347–1363.

[56] D.A. Fitri, A. Purqon, Calculation study of electric properties on molybdenum disulfide by using density functional theory, *J. Phys. Conf. Ser.* 827 (2017) 012071–012075.

[57] W. Wang, C. Yang, L. Bai, M. Li, W. Li, First-principles study on the structural and electronic properties of monolayer MoS₂ with s-vacancy under uniaxial tensile strain, *Nanomaterials* 8 (2018), 74–11.

[58] F.A. Rasmussen, K.S. Thygesen, Computational 2D materials database: electronic structure of transition-metal dichalcogenides and oxides, *J. Phys. Chem. C* 119 (2015) 13169–13183.

[59] R.M.A. Khalila, F. Hussaina, A.M. Ranaa, M. Imranb, G. Murtaza, Comparative study of polytype 2H-MoS₂ and 3R-MoS₂ systems by employing DFT, *Physica E Low Dimens. Syst. Nanostruct.* 2019 (2016) 338–345.

[60] A. Spelidiani, L. Sun, Y. Zhang, T. Li, J. Kim, C.-Y. Chim, G. Galli, F. Wang, Emerging photoluminescence in monolayer MoS₂, *Nano Lett.* 10 (2010) 1271–1275.

[61] J.D. Fuhr, A. Saúl, Scanning tunneling microscopy chemical signature of point defects on the MoS₂, *Phys. Rev. Lett.* 92 (2004) 026802–026804.

[62] S. Kc, R.C. Longo, R. Addou, R.M. Wallace, K. Cho, Impact of intrinsic atomic defects on the electronic structure of MoS₂ monolayers, *Nanotechnology* 25 (2014) 375703–375706.

[63] C.F. Matta, R.J. Boyd, *An Introduction to the Quantum Theory of Atoms in Molecules. The Quantum Theory of Atoms in Molecules: From Solid State to DNA and Drug Design*, WILEY-VCH Verlag GmbH & Co., KGaA, Weinheim, 2007.

[64] Y. Aray, D. Vega, J. Rodriguez, A.B. Vidal, D.S. Coll, Atoms in molecules theory for exploring the crystal structure and bond nature of the MoS₂ bulk, *J. Comput. Methods Sci. Eng.* 9 (2009).

[65] E. Espinosa, I. Alkorta, J. Elguero, E. Molins, From weak to strong interactions: A comprehensive analysis of the topological and energetic properties of the electron density distribution involving X–H···F–Y systems, *J. Chem. Phys.* 117 (2002) 5529–5542.

[66] P. Macchi, D.M. Proserpio, A. Sironi, Experimental electron density in a transition metal dimer: metal–metal and metal–ligand bonds, *J. Am. Chem. Soc.* 120 (1998) 13429–13435.

[67] W. Humphrey, A. Dalke, K. Schulten, VMD - Visual Molecular Dynamics, *J. Molec. Graphics* 14 (1996).